Supplementary information: Toward high-resolution NMR spectroscopy of microscopic liquid samples

Mark C. Butler,‡*[a] Hardeep S. Mehta,[a] Ying Chen,[a] Patrick N. Reardon,[ab] Ryan S. Renslow,§[a] Michael Khbeis,[c] Duane Irish,[c] and Karl T. Mueller[a]

Section S1 discusses a microslot-style detector that we initially considered using in the small-volume probe. Analysis and experimental tests suggest that signals apparently detected with the microslot[1–3] do not originate from sample in the vicinity of the slot. In Section S2, the design of the flat-wire detector and the circuit in our small-volume probe are discussed. Section S3 describes a sensitivity test of the probe, and Section S4 presents supplementary spectra mentioned in the main paper. In particular, Fig. S2 shows results obtained with a pulse sequence that yields a single peak for each aliphatic group CH_n of a biological molecule, while Fig. S3 illustrates how nonuniform sampling can be used to decrease experiment time. Materials and methods are described in Section S5.

S1 Microslot-style detector

The microslot detector[1] for small-volume NMR spectroscopy was introduced in 2007 and has since been used for metabolomic studies.[2,3] The original microslot detector was formed by laser machining a slot of width 200 μm through a copper strip of width 300 μm that rested on a planar substrate. When electric current flowing through the copper strip reaches the slot, the current is focused into the copper that remains along the sides of the slot. This focusing of the current increases the magnetic field in the vicinity of the slot, and by the principle of reciprocity,[4] detection sensitivity is enhanced in this region. Note that since the substrate supporting the copper strip has a copper plane on the back side, the microslot detector can be considered a modified microstrip transmission line.

We initially planned to use a microslot detector in our small-volume probe, and we tested one of the alternative microslot geometries presented in Ref. 1. Laser machining was used to define a narrow bridge in a wider copper strip that was fabricated by etching. The resulting detector is shown in Fig. S1.

As illustrated in the figure, a capillary placed on the copper strip can serve as a sample holder. Since the sample is not confined to the vicinity of the narrow bridge in this configuration, the detected signal includes a contribution from sample distributed along the 7-mm length of the copper strip. Simulation and experimental testing led us to the conclusion that this contribution is far larger than that of the sample located in the vicinity of the narrow bridge. Indeed, we concluded that the main effect of the laser-machined feature is to spoil the homogeneity of the static magnetic field B_0 in the central region of the copper strip. We suspect that this is also the case for previously published experiments in which a microslot detector was used.

To understand these conclusions, note first that the 7-mm copper strip shown in Fig. S1*A* is 35 times longer than the narrow bridge. If the signal per spin is 35 times larger for sample located over the bridge than for sample located over the wider copper strip, the contribution to the signal from these two regions will have the same order of magnitude. Roughly similar estimates hold for the microslot detectors described in the literature. The detector in Ref. 1 has a slot of length 100 μm in a wider copper strip of length $\sim$ 4 mm, and the microslot detectors described in Refs. 2 and 3 have similar dimensions.

Our tests with the microslot-style detector were performed at frequency 500 MHz, and the experiments with the microslot detector reported in the literature have used frequencies of 500 MHz or 600 MHz. At these frequencies, the skin depth of copper is 3 μm or less, and current flows in a thin shell at the surface of the copper. The laser-machined region focuses current because the perimeter of the cross-section is smaller in this region than at the wider strip. For the detector shown in Fig. S1, a measurement with a profilometer indicated that the copper is about 55 μm thick. The bridge is 35 μm wide, and the width of the 7-mm strip is about 110 μm. At the bridge, the perimeter of the cross-section is therefore smaller than it is at the wider strip by a factor of ~ 2. Roughly similar estimates can be made for the microslot detectors described in Refs. 1–3.

We might thus expect the rf magnetic field to be larger over the bridge by a factor of ~ 2. As illustrated in Fig. S1*C*, finite-element simulations show results consistent with this estimate. In Refs. 2 and 3, finite-element simulations show that the field is larger by a factor of ~ 3 over the microslot than over the wider strip.

Consider an NMR experiment in which a signal is detected after a single pulse flips magnetization into the transverse plane. The signal per spin in each part of the sample depends on the flip angle as well as the detector's intrinsic sensitivity. If the pulse width is optimized for detecting sample located over the laser-machined bridge or slot, then

$$\frac{\text{signal per spin over wider strip}}{\text{signal per spin over laser-machined region}} \sim x \sin(x\pi/2), \quad (1)$$

where

$$x = \frac{\text{rf field over wider strip}}{\text{rf field over laser-machined region}}. \quad (2)$$

[a] *Environmental Molecular Sciences Laboratory, Pacific Northwest National Laboratory, Richland, WA 99352. E-mail: mrkcbutler@gmail.com*
[b] *Oregon State University NMR Facility, Oregon State University, Corvallis, OR 97331.*
[c] *Washington Nanofabrication Facility, University of Washington, Seattle, WA 98195.*
‡ Present address: Halliburton Energy Services, Houston, TX 77032
§ Present address: Biological Sciences Division, Pacific Northwest National Laboratory, Richland, WA 99352

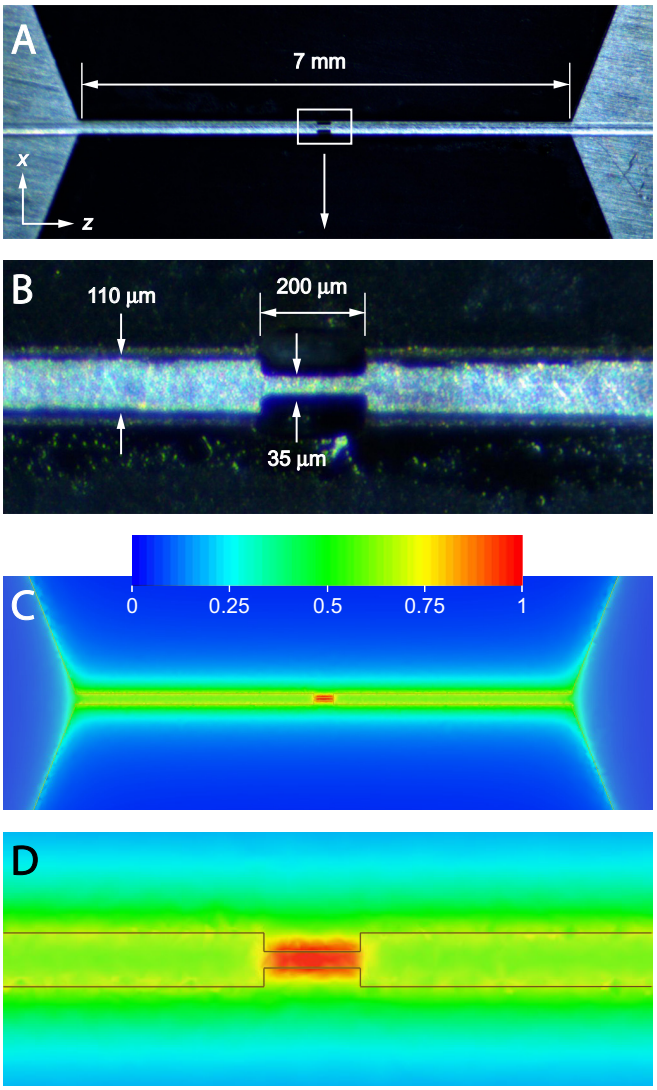

Fig. S1 Microslot detector tested in early stages of the design process. (*A*) The detector is a 7-mm copper strip with a narrow bridge at the center. The copper strip is terminated by tapered copper pads. The substrate is Rogers 5880 laminate, and there is a copper plane on the back side of the substrate. For purposes of illustration, a capillary is shown mounted on the detector. During an NMR experiment, the static magnetic field B_0 is oriented along z, and current flowing in the strip generates a linearly oscillating magnetic field along x. (*B*) A narrow bridge at the center of the strip is formed by laser micromachining. The bridge is shown without a mounted capillary. The indicated dimensions correspond to the copper surface nearest the sample during experiments. For example, the width of the copper strip at the surface facing the substrate is about $150\,\mu$m, but the width at the surface facing the capillary is about $110\,\mu$m. (*C*) A finite-element simulation of the detector's rf magnetic field shows how the field decreases away from the narrow bridge. The x component of the field is plotted at a height of $20\,\mu$m above the copper strip. (*D*) A zoomed-in view shows the variation of the field in the vicinity of the narrow bridge.

If $x \sim 1/3$, Eq. 1 implies that the signal per spin is larger by a factor of about 6 over the laser-machined region than it is over the wider strip. This factor is insufficient to compensate for the large difference in volume between the two regions.

Field inhomogeneity due to susceptibility mismatch can be expected to significantly decrease the contribution to spectroscopic signals made by sample located over the laser-machined region. When placed in a strong static magnetic field directed along z, the 7-mm detector shown in Fig. S1*A* is a long magnetized strip. If the strip were infinitely long and perfectly smooth, it would not introduce field inhomogeneity at the sample;[5] the bridge and the soldering pads are departures from this ideal geometry and thus introduce inhomogeneity. For a rough characterization of the inhomogeneity in the vicinity of the bridge, note that air replaces copper that is removed by laser ablation and that the difference between the magnetic susceptibilities of air and copper is about 10^{-5}. In a field of order 10 T, the regions in which air replaces copper can formally be considered small magnets that have magnetization $\sim 10^{-4}\,\mathrm{T}/\mu_0$. The field inside these fictitious magnets is of order 1 G, which corresponds to a proton Larmor frequency of about 4 kHz. The laser-machined regions next to the sample therefore introduce strong field gradients, and it is far from clear that these gradients will be eliminated by a shimming process that optimizes the spectroscopic signal from the capillary. We might instead expect the shimming process to enhance the spectroscopic signal contributed by sample over the wider copper strip, where the gradients associated with susceptibility mismatch are weaker.

In order to demonstrate that the signal does not originate from spins in the vicinity of the bridge, we performed NMR experiments with two detectors that were similar except at the center of the 7-mm strip. For one of these detectors, femtosecond laser ablation was used to define the bridge at the center of the strip, while for the other, no laser machining was performed, and the cross section of the strip was uniform along its length.

The same water sample, one-channel probe circuit, and pulse power were used with each detector. The one-channel circuit was obtained by disconnecting the trap and the components of the low-frequency channel from the circuit shown in Fig. 1*E* of the main paper, and the pulse power was a quarter watt. The water sample was in a capillary of inner diameter $50\,\mu$m and outer diameter $80\,\mu$m. Signal-to-noise ratio (SNR) was measured using the method described in Section S3 with a 6-s period of pulsed spin locking.

The results of these experiments are presented in Table S1. The $\pi/2$ pulse width and SNR were similar for the two detectors, but the pulse width was slightly shorter and the SNR slightly higher for the detector that did not have a laser-machined feature. These results show that the laser-machined bridge does not play a significant role in the coupling between detector and sample.

We performed a second set of experiments using only the detector with the laser-machined bridge. For these experiments, the nutation frequency was measured for three different positions of the water-filled capillary: 1) aligned with the 7-mm copper strip and resting on it, as in Fig. S1*A*, 2) transverse to the copper strip and crossing it halfway between the bridge and the end of the strip, and 3) transverse to the copper strip and crossing at the bridge.

Table S1 Comparison of the $\pi/2$ pulse width and signal-to-noise ratio for two detectors. One of the detectors has a laser-machined bridge, as shown in Fig. S1, and the other does not.

Detector design	$\pi/2$ pulse width	Single-shot SNR
with bridge	$7.25\,\mu$s	12521.5
without bridge	$6.75\,\mu$s	13073.6

Field shims were adjusted for the first of these three positions and then held fixed for the remaining positions. The nutation curves obtained with the capillary transverse to the bridge showed a contribution from spins that experienced a weak rf field at distances well removed from the strip. Because the precession frequency of these spins was shifted relative to the spins in the vicinity of the strip, however, the nutation occurring in different regions of the capillary could be distinguished. The nutation frequency of spins in the vicinity of the strip was approximately the same when the capillary was aligned with the strip as when the capillary was transverse to the strip and crossed it far from the laser-machined region. When the capillary was transverse to the strip and crossed at the bridge, weak nutation at roughly the same frequency was observed in a broadened spectral region. Referring to Figs. S1*C* and S1*D*, we can interpret these results as indicating that for all three positions of the capillary, the fast nutation occurred in the regions where the rf field is plotted in green and has amplitude roughly half the maximum value. In the small region directly over the bridge where the rf field is plotted in red and reaches its maximum value, the spectral broadening was probably too severe for nutation to be observed.

S2 Flat-wire detector and probe circuit

The analysis and experiments described in Section S1 led us to omit the laser-machined feature from the detector design. The resulting detector is a flat wire resting on a substrate that has a copper plane on the back side. Note that the substrate is about 3 mm thick, as in published microslot designs.[2,6] With the detector separated by many times its width from the copper plane, the plane can plausibly be modeled as a distinct circuit element, rather than as part of a microstrip transmission line. Simulations performed with FastHenry[7] showed that the field generated by current in the flat wire induced current loops in the copper plane. As illustrated in Fig. 1*D* of the main paper, we removed a central vertical section of the plane from the board design in order to minimize these eddy currents. The self-inductance of the copper on the back side, as calculated by FastHenry, did not change significantly due to the removal of the central vertical section from the plane.

The two-channel probe circuit, shown as a schematic in Fig. 1*E*, is designed to give sensitive detection of ^{1}H in heteronuclear experiments that include pulses on ^{13}C. At the detection frequency of 500 MHz, the flat wire has a short electrical length. Instead of using balanced driving,[8] we minimized the electrical length separating the detector from circuit ground. Connecting the detector to ground guarantees that current rather than voltage is maximized at the detector. In Fig. 1*C*, the tapered copper pad below the detector is electrically connected to the disk-shaped brass deck, which functions as circuit ground for the probe. This configuration was chosen to minimize the electrical length separating the detector from circuit ground.

S3 Sensitivity Test

We tested the sensitivity of our probe and detection scheme using a pulse sequence that has a single $\pi/2$ pulse preceding a period of pulsed spin locking. A two-step phase cycle was used to eliminate spurious signal originating from the substrate that supports the flat-wire detector. After taking the Fourier transform of the detected transient, we calculated SNR from the root-mean-square noise floor and the height of the phased peak at frequency zero. Note that optimal sensitivity requires the use of a matched filter in processing the spin-locked transient,[9] which for a sample with a single resonance amounts to multiplying the transient by a decaying exponential and integrating. For a quick estimate of SNR, however, the ratio of peak height to noise floor is convenient.

With a water sample of volume 500 pL, the single-shot SNR was 1730 for the detector of length 1 mm in the one-channel probe circuit. With a water sample of volume 15 nL, the single-shot SNR was 6910 for the detector of length 7 mm in the two-channel probe circuit. For both measurements, π pulses were applied at intervals of 500 μs during the detection period.

S4 Spectra

Heteronuclear coherence transfer echoes can be used to develop a wide range of pulse sequences. As an illustration, Fig. S2*A* shows the heteronuclear spectrum of lactate obtained with a constant-time SHARP sequence. Although successive increments increase the period of spectroscopic evolution, the periods during which homonuclear *J* couplings are active remain constant, and so these couplings do not cause splittings in the spectrum. During the evolution period for each nucleus, heteronuclear *J* couplings are refocused with a set of π pulses. The pulse sequence therefore yields a single peak for each aliphatic group CH_n of a biological molecule. Selective excitation of aliphatic groups is achieved by means of adiabatic sech/tanh pulses applied to carbon during the preparation and mixing periods.

The methods of small-volume spectroscopy presented in the main paper give spectra in one or more indirect dimensions. The potential of nonuniform sampling[13] to decrease experiment time for such methods is illustrated by Fig. S3. Uniform sampling with 185 increments was used for the upper spectrum in the figure, while nonuniform sampling (NUS) with 93 increments was used for the lower spectrum. For this demonstration, we obtained NUS data by discarding increments from the uniformly sampled data set, rather than by performing a separate experiment. But the result shows that in favorable cases, NUS methods can significantly reduce the experiment time for these small-volume methods.

S5 Materials and Methods

S5.1 Fabrication of microslot-style detectors

Microslot-style detectors such as the one shown in Fig. S1 were fabricated in two stages. For the first stage, Advanced Circuits produced a detector board that lacked the laser-machined feature at the center of the 7-mm copper strip. Mound Laser and Photonics Center then performed femtosecond laser ablation to define the

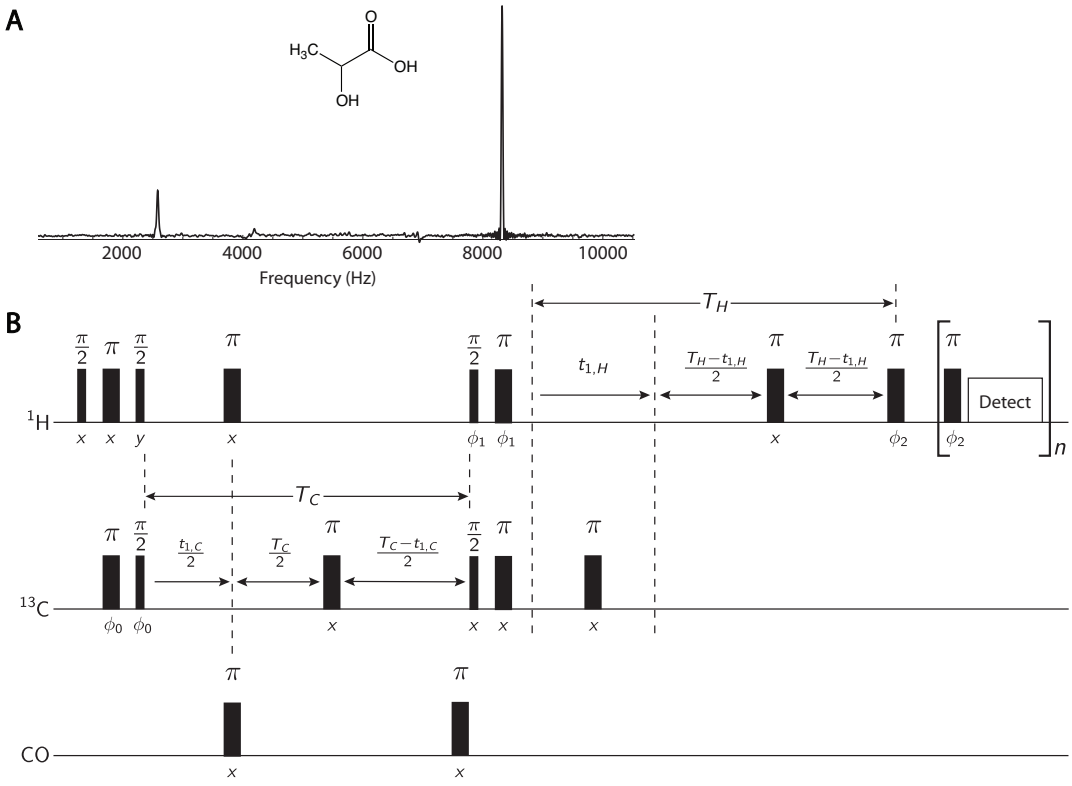

Fig. S2 Constant-time SHARP spectrum of $15\,\mathrm{nL}$ of $^{13}C_3$-labelled lactate at concentration $100\,\mathrm{mM}$. (A) The CH group and CH_3 group contribute the peaks on the left and right sides of the spectrum, respectively. Small peaks near the baseline are from impurities in the sample. The number of increments was 272, and the experiment time was $8\,\mathrm{h}$. (B) The times T_C and T_H are held constant during the experiment, while $t_{1,C} = t_1\gamma_H/(\gamma_C+\gamma_H)$ and $t_{1,H} = t_1\gamma_C/(\gamma_C+\gamma_H)$ are incremented. With an appropriate choice of selective pulses on carbon, this constant-time sequence yields a single peak for each aliphatic group CH_n of a biological molecule. For this test of the sequence, the π pulses on carbon during the preparation and mixing periods were adiabatic sech/tanh pulses giving selective inversion in the frequency range of aliphatic carbon. During the evolution period for carbon, the π pulses applied to carbon were selective for aliphatic carbon or for CO. The Q^3 pulse shape [10] was used for these selective pulses. The pulse applied to CO at the end of the evolution period for carbon compensates for pseudo-Bloch-Siegert effects caused by the previous pulse on CO. Details of the cycled phases ϕ_k are given in Section S5.

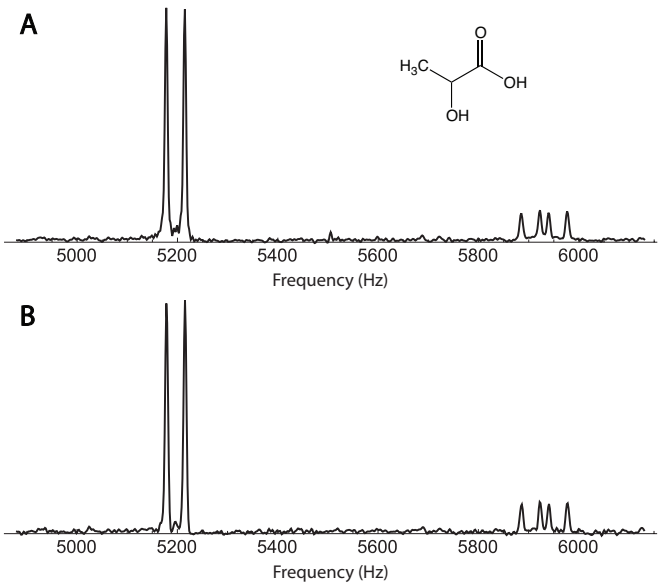

Fig. S3 Comparison of spectra obtained with uniform sampling (185 increments) and with nonuniform sampling (93 increments). (A) Uniform sampling was used for the upper spectrum, which is reproduced from Fig. 3*A* of the main paper. (B) Half of the increments of the uniformly sampled data set were selected using a randomly generated poisson-gap sampling schedule with sine-squared weighting.[11] The selected increments formed a nonuniformly sampled (NUS) data set. Processing with the SCRUB algorithm[12] to remove NUS artifacts yielded the lower spectrum, which is nearly identical to one obtained from the full data set.

narrow bridge at the center of the strip. By omitting the second stage of fabrication, we obtained detectors similar to the microslot-style detectors but lacking the laser-machined feature.

The detectors were fabricated from 1-oz copper, which has a thickness of about 35 μm, on Rogers 5880 substrate of thickness 3.175 mm. During the fabrication by Advanced Circuits, the thickness of the copper layer was increased somewhat above that of 1-oz copper. For the tests presented in Section S1, the detector that had a bridge was 54 μm thick and the detector without a bridge was 67 μm thick. For both detectors, the width of the 7-mm copper strip was about 110 μm at the surface facing the capillary and 150 μm at the surface facing the substrate.

S5.2 Fabrication of flat-wire detectors

The detector used for nanoliter samples had length 7 mm, width 100 μm, and thickness 35 μm, while the detector used for subnanoliter samples had length 1 mm, width 50 μm, and thickness 30 μm. These two detectors were designed to be used with capillaries of outer diameter 80 μm and 40 μm, respectively. Since it would be difficult or impossible to fabricate a trace of width 50 μm using conventional methods of circuit-board fabrication, novel methods were used to fabricate the two detectors.

Commercially available Rogers 5880 with copper cladding uses a roll-laminated copper foil via a thermocompression process. This approach results in significant nonuniformity in the thickness of the substrate and the conductor. Unclad Rogers 5880 was therefore used as a starting material for detector fabrication. Since most of the fabrication steps were processes conventionally used for silicon-based microfabrication, the Rogers boards were machined to disks of diameter 100 mm and thickness of 3.175 mm. The disks were cleaned using a standard solvent clean with an acetone and isopropyl alcohol sequence followed by a nitrogen drying cycle. One challenge with Rogers 5880 was that conventional microfabricated thin films had poor adhesion to the substrate surface, since it is a polytetrafluoroethylene (PTFE)-based material. The Rogers 5880 surface was activated with a reactive ion etch (RIE) process using forming gas (2% hydrogen, 98% nitrogen), which significantly enhanced adhesion of thin films.

Following surface activation, an electroplating seed layer was deposited using physical vapor deposition (PVD) techniques. The seed layer was a material stack formed of 20 nm of titanium for adhesion, 600 nm of copper as the electroplating seed, and 20 nm of titanium as a temporary oxidation barrier layer to prevent the seed metal from oxidizing during hot plate sequences.

After seed metal deposition, the substrates were patterned with positive photoresists of thickness 20 μm to 35 μm that served as an electroplating mask layer. The photoresist sequence included spin casting thick resist, an extended hot plate soft bake (since the Rogers 5880 is a poor thermal conductor), and a rehydration step for 2 hours in ambient conditions. The photoresist was then exposed using contact lithography with broad-spectrum ultraviolet light from a mercury arc lamp. The exposed resist was developed with sodium hydroxide developer followed by rinse and nitrogen drying. After measurement of critical dimensions by contact profilometry, the titanium cap was wet etched with a dilute solution of hydrofluoric acid and nitric acid to expose the copper electroplating seed. A four-point cathode fixture was used to hold the substrate, which was placed at a fixed location opposite a soluble anode in the electroplating tank with a filtered recirculating solution. Bottom-up plating was conducted until the copper overplated beyond the photoresist surface. Removal of photoresist using solvent strip was immediately followed by wet etching of the copper seed layer and the base titanium layer. These etch processes induced some surface pitting and dimension losses.

Excess copper was removed and detectors were planarized using a lapping process on cast-iron plates with progressively decreasing sizes of colloidal silica particles. The minimum particle size was 10 nm. This resulted in a surface roughness of less than 50 nm; however, lapping cannot remove sidewall pitting from the etching of the seed and adhesion layers.

Recently, for other applications, conformal seed deposition on the resist has been demonstrated followed by enhanced electroplating uniformity and trench fill using a dynamic position/rotation control electroplating system with redistribution layer (RDL) plating solutions. Trench fill processing limits topside overplating and eliminates the need for lapping. These processes are then followed by chemical mechanical polishing (CMP) to remove excess trench fill material and obtain subnanometer roughness. The use of damascene processing for future detectors could further enhance performance.

S5.3 Probe modeling and construction

The software packages used for modeling the detector and the probe circuit were ANSYS HFSS (www.ansys.com), FastHenry,[7] and Quite Universal Circuit Simulator (qucs.sourceforge.net).

Machined probe components were made by the machine shop at the Environmental Molecular Sciences Laboratory. The fixed capacitors in the probe circuit were purchased from American Technical Ceramics, and the variable capacitors were purchased from Johanson.

S5.4 Sample preparation

Samples for NMR experiments were contained in two types of capillaries. The first type, sold by VitroCom, had inner diameter (ID) 50 μm and outer diameter (OD) 80 μm. The sample volume contained in a 7-mm length of one of these capillaries was about 15 nL. For experiments with subnanoliter samples, we used capillaries that were etched to decrease wall thickness. The polymer coating was removed from capillaries TSP020090 sold by Polymicro, and the bare capillaries were etched using a process described in Ref. 14. The ID after etching was measured using a fluorescence microscope that detected fluorescein loaded into the capillaries. The capillaries had ID 20 μm and OD 70 μm before etching and ID 25 μm after etching. The sample volume contained in a 1-mm length of an etched capillary was about 500 pL.

Two different methods were used to load samples into capillaries. The simplest was to dip the capillary into the liquid sample and let capillary action bring the sample into the capillary. Samples could also be injected into capillaries using a Hamilton syringe together with fittings (union, injection port, and liner). With both methods, the capillaries were sealed with wax after the sample was loaded. For NMR experiments, a sealed capillary was manually positioned on the detector with the aid of a microscope and then fixed in place with tape.

S5.5 Configuration of spectrometer and probe

A Bruker Avance III NMR spectrometer and a Varian NMR spectrometer from Agilent Technologies were used for small-volume NMR experiments. Both spectrometers have an 11.7-T magnet with an 89-mm vertical bore.

The Varian spectrometer is normally configured for solid-state NMR, and its configuration needed to be modified for experiments with the small-volume probe. One of the two amplifiers normally used in series for the ^{1}H channel was bypassed, and the remaining amplifier was used to apply low-power pulses. In the ^{13}C channel, attenuators were used to decrease pulse power by 26 dB. Noise-figure measurements showed that the attenuators in the ^{13}C channel did not add noise to signals detected in the ^{1}H channel.

With pulse power in the ^{1}H channel at a quarter watt, typical $\pi/2$ pulse widths obtained with the detectors of length 1 mm and length 7 mm were 2.9 μs and 6.75 μs, respectively. Attenuated high-power pulses on carbon using the 7-mm detector typically gave $\pi/2$ pulse widths of about 7 μs.

For experiments on the Varian spectrometer, an air flow of 30 L/min at 25 °C was used for temperature regulation. Rather than systematically testing to find the minimum air flow needed for temperature regulation, we used an air flow that was typical for the spectrometer. The air flow was decreased to 5 L/min for experiments on the Bruker spectrometer. Temperature changes during pulsed spin locking were monitored using methanol samples and found to be insignificant ($\lesssim 1$ °C).

S5.6 Shimming

Although a shimmed field was not essential for spectral resolution, shimming facilitated the calibration of pulse-sequence parameters. For experiments on the Varian spectrometer, coarse manual shimming gave a relatively narrow feature in the water peak (e.g., a linewidth of 15 Hz to 30 Hz at half height for the detector of length 7 mm). For some experiments on the Bruker spectrometer, iterative automated shimming was performed with ParaVision AdjShim, following the simplex method up to second-order shim sets (xz, yz, x^2+y^2, xy, and z^2). Five sets of shimming were completed consecutively. The first shimming set consisted of first-order shims (x, y, and z), with three stabilization scans between adjustment, and 87 total adjustment steps. Steps started with an initial range of 100%, but the range sequentially decreased following an exponential decay to a final range of 1%. The second shim set consisted of first-order and second-order shims, alternating between the full first-order shims and a subset of the second-order shims. Two stabilization scans were used between adjustment, with a total of 250 total adjustment steps. Steps started with an initial range of 25%, but the range sequentially decreased following an exponential decay to a final range of 1%. The third, fourth, and fifth shim sets were alternations between the first-order-only method, and the first/second-order method, with decreasing adjustment ranges. The final adjustment was the z shim with an adjustment step size of only 0.05%. Improving magnetic field homogeneity was monitored using the single-pulse method. After shimming, the signal-to-noise ratio improved by a factor of 3.3, the peak width at half height decreased by a factor of 18.7, and the peak width at the base of the peak (10% height) decreased by a factor of 3.6. For the 7-mm detector, automated shimming gave a width of 10 Hz or below at half height.

S5.7 Sensitivity test

Sensitivity was measured using a pulse sequence in which a single $\pi/2$ pulse is followed by a period of pulsed spin locking. A single shot of this pulse sequence yields a decaying transient of spin-locked magnetization.

In the absence of any phase cycling, we found that after each π pulse applied during the detection period, the transient showed a spike that decayed in tens of microseconds. We believe that these quickly decaying spikes originate from ^{1}H nuclei in the substrate that supports the detector. A two-step phase cycle eliminated these spikes. The receiver phase and the phase of the initial $\pi/2$ pulse were held constant, and the phase of the pulses applied during the detection period was changed by π radians between transients.

Detection sensitivity was estimated from the Fourier transform of the phase-cycled transient. The estimate of single-shot SNR was

$$\mathrm{SNR} = \frac{\text{height of phased peak at frequency zero}}{\sqrt{2}\,(\text{rms noise floor})}, \qquad (3)$$

where the factor of $\sqrt{2}$ in the denominator takes account of the fact that two transients were summed during the phase cycle.

For the SNR measurements reported in Section S3, the time interval between the center of successive π pulses during the detection period was 500 μs. The period of pulsed spin locking lasted 6 s and 3 s for the detectors of length 7 mm and 1 mm, respectively.

S5.8 Homonuclear spectrum

A continuous-wave saturation pulse of duration 60 ms and power 1 μW was used for water suppression at the beginning of the zero-quantum pulse sequence. The recycle delay between transients was 3 s. During the detection period, which lasted 1 s, the time interval between the center of successive π pulses was 200 μs. The number of increments was 2048, and the spectral width associated with the increment was 3 kHz. The preparation and mixing periods each lasted 60 ms.

An eight-step phase cycle was used in the pulse sequence. Phase ϕ_0 shown in Fig. 2*B* was varied in a four-step cycle $\{x, y, -x, -y\}$ that eliminated pathways for which the pulses of the preparation period cause a change in coherence order. During the detection period, an independent two-step cycle $\{y, -y\}$ of phase ϕ_1 eliminated spurious signal originating from the substrate that supports the flat-wire detector. The receiver phase was constant during the experiment.

S5.9 Heteronuclear spectra

In presenting details of SHARP experiments, we use "plain SHARP," "J SHARP," and "constant-time SHARP" to refer to the respective pulse sequences presented in Figs. 3 and 4 of the main paper and in Fig. S2 of this supporting information.

These pulse sequences include separate evolution periods for ^{1}H and for ^{13}C. During each evolution period, an inversion pulse is applied to the nonprecessing nucleus to refocus heteronuclear J couplings. The composite pulse $90_0240_{90}90_0$ [15] was used for these inversion pulses. For plain SHARP and J SHARP, the same composite inversion pulse was applied to carbon during the preparation and mixing periods. For constant-time SHARP, the π pulses applied to carbon during the preparation and mixing periods were adiabatic sech/tanh pulses giving selective inversion in the frequency range of aliphatic carbon. During the constant-time evolution period for carbon, the Q^3 pulse shape [10] was used for the selective π pulses applied to aliphatic carbon and to CO.

For the sequences in which a composite pulse was applied to carbon during the preparation and mixing periods, the duration of each of these periods was 3.54 ms. This duration was increased slightly for the constant-time SHARP experiment in order to take account of the scaling of J couplings during the adiabatic pulse. [16] The respective lengths of the detection periods for plain SHARP, constant-time SHARP, and J SHARP were 1 s, 0.5 s, and 0.25 s. The respective recycle delays were 2 s, 1.1 s, and 1.2 s. For constant-time SHARP, the times T_C and T_H shown in Fig. S2*B* were 27.8 ms and 6.8 ms, respectively.

During the detection period of SHARP sequences that yielded a one-dimensional spectrum, the time interval between the center of successive π pulses was 100 μs. In order to prevent sample heating as π pulses were applied both to carbon and to proton, this time was increased to 250 μs for J SHARP. The time increment used for constant-time SHARP was $\Delta t_1 = 125\,\mu$s, and the number of increments was 272. Plain SHARP and J SHARP had $\Delta t_1 = 1$ ms, with 185 and 225 increments, respectively.

For the display of SHARP spectra, the frequency axis corresponding to evolution in the indirect dimension was scaled to show $\nu_C - \nu_H\,(\gamma_C/\gamma_H)$, where ν_C and ν_H are the respective chemical-shift offset frequencies of the ^{13}C and ^{1}H nuclei in a CH$_n$ group, with γ_C and γ_H the respective gyromagnetic ratios. Note that with this convention, the time increment $\Delta t_1 = 1$ ms gives a spectral width of 1.25 kHz. Fig. S2*A* shows that the SHARP frequencies for the CH$_3$ and CH groups of lactate are separated by ~ 5.7 kHz. In Figs. 3*A* and 4*B*, the peaks for these two groups are folded into a spectral width of 1.25 kHz centered on 5.5 kHz.

Plain SHARP and J SHARP used the same 32-step phase cycle. The phases ϕ_0 and ϕ_1 shown in Figs. 3*B* and 4*C* changed together in a four-step cycle $\{x, y, -x, -y\}$ that selected the coherence transfer echo. There were also three independent two-step cycles $\{x, -x\}$: a cycle of ϕ_0 together with the receiver phase, which suppressed pathways having a change in coherence order of 0 or ± 2 due to the preparation pulses on carbon; a cycle of ϕ_2, which eliminated artifacts caused by imperfect inversion of carbon during the precession period for proton; and a cycle of ϕ_3, which eliminated spurious signal originating from the substrate that supports the detector. Constant-time SHARP used a 16-step cycle that differed from the 32-step cycle in using a fixed phase x for the π pulse applied to carbon during the evolution period for proton.

For J SHARP, a two-dimensional absorption spectrum was obtained by applying a short burst of spin-lock pulses to proton at the beginning of the detection period. The spin-lock pulses, which dephased one quadrature component of the magnetization and selected the other as the starting state for evolution in the direct dimension, were applied along different axes for successive transients.

Conventional high-resolution one-dimensional spectra of the lactate samples used for SHARP experiments showed that impurities were present, and these were assumed to be responsible for the small peaks close to the baseline in SHARP spectra. Tests of plain SHARP involving a range of different phase cycles showed that these peaks were not artifacts caused by pulse imperfections.

S5.10 Data processing

Processing of a spin-locked transient yields one quadrature component of the transverse magnetization present at the beginning of the detection period. The processing should filter noise to determine the initial amplitude of a signal composed of decaying exponentials. If the functional form of a signal is known, the optimal filter for finding the signal amplitude in the presence of white noise is a matched filter. [17] For our experiments, the detected signal was a sum of decaying exponentials, but the exact functional form was not known. As an approximation to a matched filter, a single decaying exponential was used in processing. Multiplying a transient by the decaying exponential and then integrating gave an estimate

(in arbitrary units) of the spin-locked magnetization at the beginning of the detection period.

The J SHARP spectrum had t_1 ridges running parallel to the F_1 axis through the strong peaks generated by the CH_3 group of lactate. These ridges were eliminated by averaging a set of F_2 spectra that showed only the ridges and then subtracting the average from each F_2 spectrum of the data set.[18]

S5.11 Nonuniform sampling

A nonuniformly sampled (NUS) data set was generated from uniformly sampled data that had been processed to yield a single complex point for each increment. These complex points represented the evolution of magnetization in the indirect dimension. A randomly generated poisson-gap sampling schedule with sine-squared weighting[11] was used to select half of the increments to be included in the NUS data. For the increments that were not selected, the complex data point representing sampled evolution was set to zero. Fourier transform and baseline correction of NUS data were performed with NMRPipe,[19] and the SCRUB algorithm for removing NUS artifacts[12] was implemented using *nmr_wash* (coggins.biochem.duke.edu/scrub), a suite of software tools.

References

1 Y. Maguire, I. L. Chuang, S. Zhang and N. Gershenfeld, *Proc. Natl. Acad. Sci. U. S. A.*, 2007, **104**, 9198–9203.

2 H. G. Krojanski, J. Lambert, Y. Gerikalan, D. Suter and R. Hergenröder, *Anal. Chem.*, 2008, **80**, 8668–8672.

3 A. Kalfe, A. Telfah, J. Lambert and R. Hergenröder, *Anal. Chem.*, 2015, **87**, 7402–7410.

4 J. J. van der Klink, *J. Magn. Reson.*, 2001, **148**, 147 – 154.

5 P. J. M. van Bentum, J. W. G. Janssen, A. P. M. Kentgens, J. Bart and J. G. E. Gardeniers, *J. Magn. Reson.*, 2007, **189**, 104 – 113.

6 Y. G. E. Maguire, *Ph.D. thesis*, Massachusetts Institute of Technology, 2004.

7 M. Kamon, M. J. Tsuk and J. K. White, *IEEE Trans. Microwave Theory Tech.*, 1994, **42**, 1750–1758.

8 F. Engelke, *Concepts Magn. Reson.*, 2002, **15**, 129–155.

9 M. C. Butler and D. P. Weitekamp, *Phys. Rev. B*, 2013, **87**, 064413.

10 L. Emsley and G. Bodenhausen, *J. Magn. Reson. (1969)*, 1992, **97**, 135 – 148.

11 S. G. Hyberts, K. Takeuchi and G. Wagner, *J. Am. Chem. Soc.*, 2010, **132**, 2145–2147.

12 B. E. Coggins, J. W. Werner-Allen, A. Yan and P. Zhou, *J. Am. Chem. Soc.*, 2012, **134**, 18619–18630.

13 M. Mobli, M. W. Maciejewski, A. D. Schuyler, A. S. Stern and J. C. Hoch, *Phys. Chem. Chem. Phys.*, 2012, **14**, 10835–10843.

14 R. T. Kelly, J. S. Page, Q. Luo, R. J. Moore, D. J. Orton, K. Tang, and R. D. Smith, *Anal. Chem.*, 2006, **78**, 7796–7801.

15 R. Freeman, S. P. Kempsell and M. H. Levitt, *J. Magn. Reson. (1969)*, 1980, **38**, 453 – 479.

16 M. Bendall, *J. Magn. Reson., Ser. A*, 1995, **116**, 46 – 58.

17 L. A. Wainstein and V. D. Zubakov, *Extraction of Signals from Noise*, Dover, New York, 1962.

18 R. E. Klevit, *J. Magn Reson (1969)*, 1985, **62**, 551 – 555.

19 F. Delaglio, S. Grzesiek, G. W. Vuister, G. Zhu, J. Pfeifer and A. Bax, *J. Biomol. NMR*, 1995, **6**, 277–293.